A&A 663, A141 (2022)
https://doi.org/10.1051/0004-6361/202142768

Astronomy & Astrophysics

The GAPS Programme at TNG

XXXIII. HARPS-N detects multiple atomic species in emission from the dayside of KELT-20b*

F. Borsa[1], P. Giacobbe[2], A. S. Bonomo[2], M. Brogi[3,2,4], L. Pino[5], L. Fossati[6], A. F. Lanza[7], V. Nascimbeni[8], A. Sozzetti[2], F. Amadori[2], S. Benatti[9], K. Biazzo[10], A. Bignamini[11], W. Boschin[12,13,14], R. Claudi[8], R. Cosentino[12], E. Covino[15], S. Desidera[8], A. F. M. Fiorenzano[12], G. Guilluy[2], A. Harutyunyan[12], A. Maggio[9], J. Maldonado[9], L. Mancini[16,17,2], G. Micela[9], E. Molinari[18], M. Molinaro[11], I. Pagano[7], M. Pedani[12], G. Piotto[19], E. Poretti[1,12], M. Rainer[5], G. Scandariato[7], and H. Stoev[12]

[1] INAF – Osservatorio Astronomico di Brera, Via E. Bianchi 46, 23807 Merate (LC), Italy
e-mail: francesco.borsa@inaf.it
[2] INAF – Osservatorio Astrofisico di Torino, Via Osservatorio 20, 10025 Pino Torinese, Italy
[3] Department of Physics, University of Warwick, Coventry CV4 7AL, UK
[4] Centre for Exoplanets and Habitability, University of Warwick, Gibbet Hill Road, Coventry CV4 7AL, UK
[5] INAF – Osservatorio Astrofisico di Arcetri, Largo E. Fermi 5, 50125 Firenze, Italy
[6] Space Research Institute, Austrian Academy of Sciences, Schmiedlstrasse 6, 8042 Graz, Austria
[7] INAF – Osservatorio Astrofisico di Catania, Via S. Sofia 78, 95123, Catania, Italy
[8] INAF – Osservatorio Astronomico di Padova, Vicolo dell'Osservatorio 5, 35122 Padova, Italy
[9] INAF – Osservatorio Astronomico di Palermo, Piazza del Parlamento, 1, 90134 Palermo, Italy
[10] INAF – Osservatorio Astronomico di Roma, via Frascati 33, I00040 Monte Porzio Catone (RM), Italy
[11] INAF – Osservatorio Astronomico di Trieste, via Tiepolo 11, 34143 Trieste, Italy
[12] Fundación Galileo Galilei - INAF, Rambla José Ana Fernandez Pérez 7, 38712 Breña Baja, TF, Spain
[13] Instituto de Astrofísica de Canarias (IAC), C/Vía Láctea s/n, 38205 La Laguna, TF, Spain
[14] Departamento de Astrofísica, Universidad de La Laguna (ULL), 38206 La Laguna, TF, Spain
[15] INAF – Osservatorio Astronomico di Capodimonte, Salita Moiariello 16, 80131 Napoli, Italy
[16] Department of Physics, University of Rome Tor Vergata, Via della Ricerca Scientifica 1, 00133 Rome, Italy
[17] Max Planck Institute for Astronomy, Königstuhl 17, 69117 Heidelberg, Germany
[18] INAF – Osservatorio di Cagliari, via della Scienza 5, 09047 Selargius, CA, Italy
[19] Dip. di Fisica e Astronomia Galileo Galilei – Università di Padova, Vicolo dell'Osservatorio 2, 35122 Padova, Italy

Received 27 November 2021 / Accepted 10 April 2022

ABSTRACT

The detection of lines in emission in planetary atmospheres provides direct evidence of temperature inversion. We confirm the trend of ultra-hot Jupiters orbiting A-type stars that show temperature inversions on their daysides by detecting metals emission lines in the dayside of KELT-20b. We first detected the planetary emission by using the G2 stellar mask of the HARPS-N pipeline, which is mainly composed of neutral iron lines, as a template. Using neutral iron templates, we performed a retrieval of the atmospheric temperature-pressure profile of the planet, confirming a thermal inversion. Then we created models of planetary emission of different species using the retrieved inverted temperature-pressure profile. By using the cross-correlation technique, we detected Fe I, Fe II, and Cr I at signal-to-noise ratio levels of 7.1, 3.9, and 3.6, respectively. The latter was detected in emission in the atmosphere of an exoplanet for the first time. Contrary to Fe I, Fe II and Cr I were detected only after the occultation and not before, hinting at different atmospheric properties in view during the pre- and post-occultation orbital phases. A further retrieval of the temperature-pressure profile performed independently during the pre- and post-occultation phases, while not highly significant, points to a steeper thermal inversion in the post-occultation.

Key words. techniques: spectroscopic – planets and satellites: atmospheres – planetary systems – stars: individual: kelt-20

1. Introduction

Ultra-hot Jupiters (UHJs) are highly irradiated gas giant planets with equilibrium temperatures exceeding 2000 K and hosting atmospheres presenting substantial H_2 dissociation and H^- opacity (e.g., Arcangeli et al. 2018; Parmentier et al. 2018; Bell & Cowan 2018). They show different atmospheric properties from the classic hot Jupiters. In particular, one key characteristic is the atmospheric thermal inversion, which appears to happen when the equilibrium temperature reaches ~1700 K, with observational evidence for a transition between the two regimes (Baxter et al. 2020). Fossati et al. (2021) show that non-local thermodynamic equilibrium (non-LTE) effects play a significant

* Based on observations made with the Italian Telescopio Nazionale Galileo (TNG) operated on the island of La Palma by the Fundacion Galileo Galilei of the INAF at the Spanish Observatorio Roque de los Muchachos of the IAC in the frame of the programme Global Architecture of the Planetary Systems (GAPS).

role in determining the shape of the temperature inversion. While previous studies predicted the temperature inversion to be mainly caused by TiO and VO (e.g., Hubeny et al. 2003; Fortney et al. 2008), more recent works have shown that also the presence of atomic species (e.g., Fe and Ti) alone (coupled with the thermal dissociation of infrared coolants such as H_2O) can cause atmospheric inversions (e.g., Lothringer et al. 2018; Lothringer & Barman 2019). Lothringer & Barman (2019) suggest that UHJs can have a temperature inversion originating from atomic absorption depending on the stellar spectral type. This presence of atomic species has been observationally confirmed with high-resolution spectroscopy, mainly in transmission (e.g., Hoeijmakers et al. 2019; Kesseli et al. 2020; Gibson et al. 2020; Borsa et al. 2021).

High-resolution spectroscopy allows us to distinguish between the planetary and stellar spectrum, owing to the time-resolved Doppler shift due to the planetary orbital motion. Moreover, it enables us to resolve individual lines, ensuring the unambiguous detection of atomic and molecular species. High-resolution emission spectroscopy can aid in the determination of the primary thermal inversion causing opacity sources. After the first detection of neutral iron emission from the dayside of a UHJ (KELT-9b, Pino et al. 2020, confirmed in Kasper et al. 2021), neutral iron in emission has since been detected at high resolutions in WASP-33b (Nugroho et al. 2020a) and in WASP-189b (Yan et al. 2020), which are two other UHJs orbiting A-type stars.

KELT-20b (Lund et al. 2017), also known as MASCARA-2b (Talens et al. 2018), is a UHJ ($T_{\rm eq}$ ~ 2200 K) orbiting a fast-rotating ($v \sin i$ ~ 116 km s^{-1}) A2-type star in ~3.5 days. Its atmosphere is the subject of many investigations, with high-resolution transmission spectroscopy leading to the detection of different species such as Na, H, Mg, Fe I, Fe II, Ca II, Cr, and possibly FeH (Casasayas-Barris et al. 2018, 2019; Stangret et al. 2020; Nugroho et al. 2020b; Hoeijmakers et al. 2020a; Kesseli et al. 2020). The Fe I features have been further used to detect the atmospheric Rossiter-McLaughlin effect (Rainer et al. 2021) and to provide evidence of probable atmospheric variability (Nugroho et al. 2020b; Rainer et al. 2021). The chemical composition of the host star was also recently derived (Saffe et al. 2021).

In this work we present the high-resolution detection of multiple species in emission from the dayside of KELT-20b, suggesting the presence of an atmospheric thermal inversion. In Sect. 2 we present our dataset, and in Sect. 3 the detection of emission from the planet. We then perform a T-P profile retrieval in Sect. 4, search for emission from different atomic species in Sect. 5, and conclude with a discussion and final remarks in Sect. 6.

2. Data sample

In the framework of the GAPS programme (Borsa et al. 2019; Guilluy et al. 2020; Giacobbe et al. 2021), we observed KELT-20 with the HARPS-N and GIANO-B high-resolution spectrographs, mounted at the Telescopio Nazionale Galileo. We used the GIARPS configuration (Claudi et al. 2017), which allowed us to simultaneously use the two spectrographs, obtaining high-resolution spectra in the wavelength range ~390–690 nm and ~940–2420 nm. In this work, we analyse only the HARPS-N spectra, leaving the analysis of the GIANO-B ones to another work. We observed both pre- (0.4–0.44) and post-eclipse (0.52–0.59) phases, where 0.0 and 0.5 correspond to the transit and secondary eclipse phases, respectively, with integrations of 600 s for each spectrum. While fibre A of the spectrograph was centred on the target, fibre B was monitoring the sky simultaneously. The weather conditions on both nights suffered from calima. A log of the observations is reported in Table 1.

Table 1. KELT-20b HARPS-N observations log.

Night #	Night [(1)]	Phase	$N_{\rm obs}$	Airmass	$S/N_{\rm ave}$
1	11 Oct 2020	0.53–0.59	30	1.0–2.5	165
2	14 Oct 2020	0.40–0.44	25	1.1–2.0	200

Notes. [(1)]Start of night civil date.

3. Planetary emission detection

In order to check if the planetary Doppler trail was present (Fig. 1), we started our analysis from the stellar cross-correlation functions (CCFs) extracted by version 3.7 of the HARPS-N Data Reduction Software (DRS) pipeline (Cosentino et al. 2014), using the YABI interface with custom parameters (e.g., Borsa et al. 2015). In particular, we used a G2 stellar mask (the mask already rejects regions strongly contaminated by tellurics), and we enlarged the CCF width to the range [−300:300] km s^{-1}. This was done to take the large $v \sin i$ of the star into account and to sample the velocity range of the possible planetary signal, which is expected to appear offset from the stellar velocity by dozens of km s^{-1} at the observed orbital phases. The stellar mask used to compute the CCF is mainly composed of Fe I lines (Ehrenreich et al. 2020), and it is thus a good template for searching for neutral iron in the planetary atmosphere.

We analysed each of the two nights of observations (Table 1) independently. We first shifted the CCFs into the stellar rest frame using the Keplerian orbital solution calculated with the parameters of Table A.1. The CCFs suffered from an evident slope, due to the imperfect colour correction caused by the spectral type of the star, which does not have a proper colour correction template. We thus normalised the CCFs by dividing for a linear fit performed excluding the range [−140:140] km s^{-1} (i.e., we fitted only the continuum). Then we created a master CCF ($\rm CCF_{master}$) by determining the median of all the CCFs, and we divided all the CCFs for this $\rm CCF_{master}$.

This normalisation allowed us to null the largely stationary stellar spectrum, but not the planetary one, which shifts across numerous different pixels over the course of the observing sequence. The median approach has been successfully used in other works involving planetary emission (Pino et al. 2020) and reflectance spectroscopy (Scandariato et al. 2020). At this stage in the analysis process, the planetary Doppler trail within the CCF residuals was weakly present (Fig. 1, left panels).

For a range of $K_{\rm p}$ values from 0 to 300 km s^{-1}, in steps of 1 km s^{-1}, we averaged the $\rm CCF_{res}$ shifted in the planetary rest frame, which was done by subtracting the planetary radial velocity computed for each exposure as $v_{\rm p} = K_{\rm p} \times \sin 2\pi\phi$, with ϕ being the orbital phase. We thus created the $K_{\rm p}$-$\Delta V_{\rm sys}$ maps – with $\Delta V_{\rm sys}$ being the difference from the literature reported systemic velocity $V_{\rm sys}$ – which we used to check the presence of a significant signal close to the expected planetary $K_{\rm p}$ (Fig. 1, central panels). We then looked at the signal at the nominal $K_{\rm p}$ (i.e., at the row of the $K_{\rm p}$-$\Delta V_{\rm sys}$ map corresponding to $K_{\rm p}$ = 175 km s^{-1}), and we performed a 1D Gaussian fit to measure its amplitude (Fig. 1, right panels).

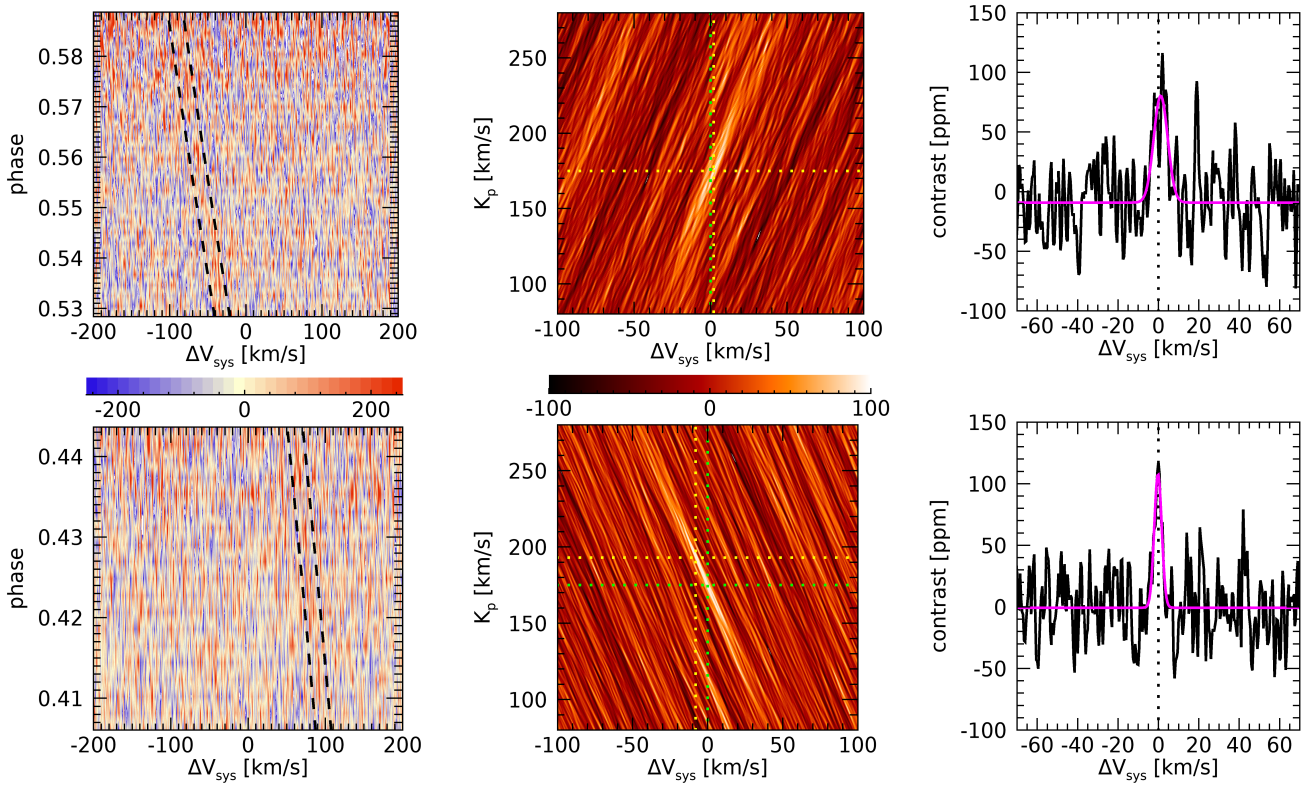

Fig. 1. CCF signal of KELT-20b. The first row refers to night 1 and the second row to night 2. *Left panels*: 2D tomography of the CCF residuals maps. The dashed lines bracket the expected planetary signal position. *Central panels*: K_p-ΔV_{sys} maps. The green dotted lines mark the theoretical planetary position. *Right panels*: planetary emission signal averaged at the theoretical K_p. The magenta line represents the Gaussian fit to the data.

Table 2. KELT-20b emission detections with the stellar G2 mask as a template.

Night	Contrast [ppm]	Centre [km s^{-1}]	$FWHM$ [km s^{-1}]
1	89 ± 10	1.1 ± 0.5	8.1 ± 1.1
2	108 ± 12	−0.2 ± 0.2	4.3 ± 0.7

There is a significant detection of planetary emission for both nights, with signal-to-noise ratio (S/N) levels of 3.2 and 4.0 for night 1 and night 2, respectively. The S/N of the detections was calculated with respect to the noise level of the continuum (~27–28 ppm on both nights), which was evaluated by calculating the standard deviation of the K_p-ΔV_{sys} maps far from where any stellar or planetary signal is expected. The planetary signal was detected in emission (i.e., opposite to the stellar signal, which is in absorption), which is an unambiguous sign of thermal inversion in its atmosphere (Pino et al. 2020). Without thermal inversion, the signal would have been seen in absorption (i.e., a negative signal). The results of the Gaussian fits are shown in Table 2, expressed as the ratio between the planetary and stellar flux. The amplitudes of the planetary signal at the theoretical K_p are consistent for both nights, but there is a difference in their full widths at half maximum (FWHMs). We note that pre- and post-occultation orbital phases show different regions of the planetary atmosphere, and any difference because of a non-identical temperature, chemical composition, and abundances is indeed possible. By using the theoretical K_p for two different nights and different orbital phases, we intrinsically assume a circular Keplerian orbit and that there is no atmospheric dynamics influencing the observed velocities. This latter point, in particular, has been questioned by recent results on this planet, which show possible variability of the K_p detected in transmission with an iron mask (Nugroho et al. 2020b; Rainer et al. 2021). Comparing, in detail, the results of different nights taken at different orbital phases to constrain the 3D characteristics of a planetary atmosphere requires a more complex 3D modelling analysis framework. Such a framework is out of the scope of this manuscript and will be the subject of another work (Pino et al., in prep.).

We then combined the K_p-ΔV_{sys} maps from each night (Fig. 2) by summing them. We also fitted the signal resulting from the combination with a 2D Gaussian, obtaining values of $K_p = 173 \pm 9$ km s^{-1} and $\Delta V_{sys} = 0.6 \pm 3.6$ km s^{-1}.

4. T-P profile retrieval

In order to constrain the T-P profile, we performed an atmospheric retrieval following a framework similar to that presented in Yan et al. (2020), using the same likelihood function as presented in Gibson et al. (2020). After normalising the stellar spectra, we corrected for tellurics by exploiting the relation between their depth and airmass (e.g., Snellen et al. 2008; Vidal-Madjar et al. 2010). Then we created a master stellar spectrum by shifting the spectra in the stellar rest frame and taking a median spectrum. The orbital velocity of the planet coupled with the instrumental resolution ensures that the planetary signal was removed from this master spectrum (e.g., Scandariato et al. 2020). All the spectra were then normalised for this master stellar spectrum, and all the residual spectra S_{res} were shifted in the planetary rest frame using the theoretical K_p value, which we assume to be fixed. This K_p value was also confirmed by our

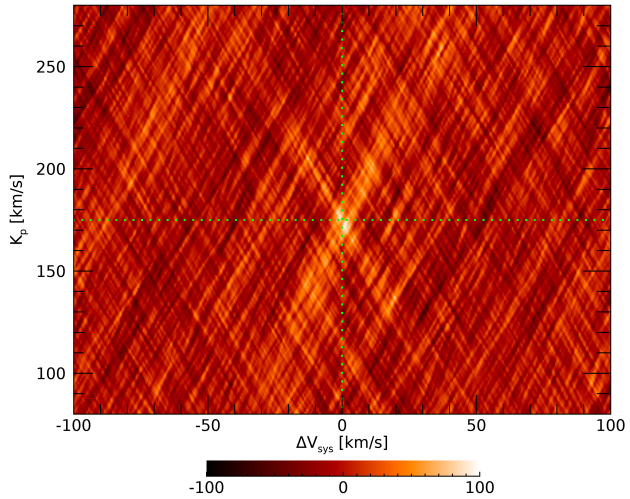

Fig. 2. K_p-ΔV_{sys} map of the two nights combined. The green dotted lines mark the expected planetary position at K_p = 175 km s^{-1}. The colour scale is in ppm.

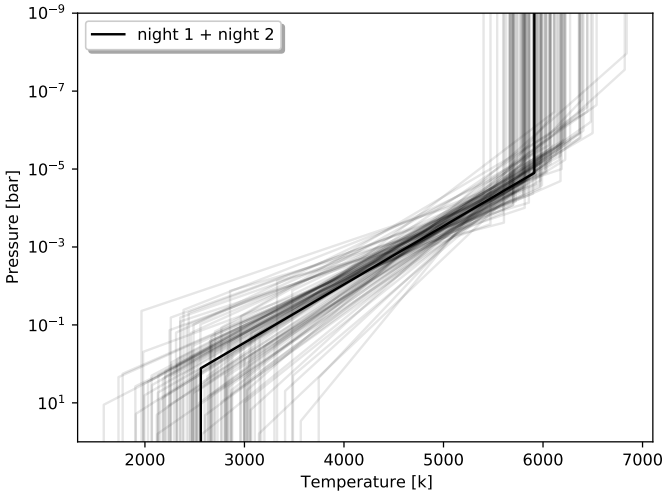

Fig. 3. T-P profile retrieved for the dayside of KELT-20b in this work. Thinner lines represent 100 T-P profiles randomly extracted from the MCMC posteriors.

analysis of Sect. 3. The residual spectra of both nights were then merged together with a weighted average, creating the final planetary spectrum R_i. The error bar on the flux of each wavelength point σ_i was calculated on the stellar spectrum as the square root of the flux, and then propagated through the analysis.

The detection of the stellar CCF in emission at the planetary K_p proved the presence of neutral iron in the planet (Sect. 3). We then performed the retrieval by generating neutral iron emission model spectra for the planetary atmosphere with `petitRADTRANS` (Mollière et al. 2019), assuming solar metallicity and equilibrium chemistry. Following Yan et al. (2020), we considered a two-point T-P profile (Fig. 3). The temperature in the atmosphere below the higher pressure point and beyond the lower pressure point was considered to be isothermal, and the slope between the two points was defined by a gradient

$$T_{\rm slope} = \frac{T_2 - T_1}{\log_{10} P_2 - \log_{10} P_1}, \quad (1)$$

with the temperature changing linearly with $\log_{10} P$. The generated model spectra were then divided for a stellar blackbody spectrum with $T_{\rm eff}$ = 8980 K (Table A.1) to have the model in units of F_p/F_s, convolved with the instrumental profile (using a resolving power of 115 000), and were continuum normalised. When using a stellar blackbody spectrum, we ignored the dependence on the stellar lines.

For the T-P profile retrieval, we used the wavelength range 4000–6500 Å, discarding the low S/N bluer wavelengths and the heavily telluric affected red ones. The retrieval was performed in a Bayesian framework by employing a differential evolution Markov chain Monte Carlo (DE-MCMC) technique (Ter Braak 2006; Eastman et al. 2013), running ten DE-MCMC chains. We left $\log_{10} P_1$, T_1, $\log_{10} P_2$, T_2, and ΔV_{sys} as free parameters for which we set uninformative priors. For the identification of the burn-in steps and the convergence and well-mixing of the DE-MCMC chains, we followed the same criteria as in Eastman et al. (2013). We took the medians and the 15.86 and 84.14% quantiles of the posterior distributions as the best values and 1σ uncertainties of the model parameters. By parallelising our retrieval code, we were able to reduce the computing time and to generate models in continuum, without using a grid as in Yan et al. (2020). This means that a new model of iron in the atmosphere was computed at each step of each chain. The best retrieved values are shown in Table 3, with the best T-P profile from the retrieval shown in Fig. 3 and the corner plot with the MCMC posterior distributions in Fig. 4.

Table 3. Results of the T-P profile retrieval.

Parameter	Value	Unit
ΔV_{sys}	$1.71^{+0.28}_{-0.26}$	km s^{-1}
$\log_{10} P_1$	$-0.11^{+0.93}_{-0.85}$	log bar
T_1	$2561.38^{+385.73}_{-425.84}$	K
$\log_{10} P_2$	$-4.90^{+0.54}_{-0.58}$	log bar
T_2	$5912.93^{+244.21}_{-225.64}$	K

5. Searching for atomic species

Once the T-P profile was determined using Fe I models, we checked for the presence of emission from other species. We looked first at Fe I, as in the retrieval, to confirm that this is the main source of the detection with the stellar mask. Then we also looked for Fe II, Ti I, and Cr I, which are among the other principal components of the stellar mask (e.g., Ehrenreich et al. 2020).

Emission model spectra for the planetary atmosphere were generated in the same way as in Sect. 4, using the retrieved T-P profile. The Fe I, Ti I, and Cr I models present many emission lines, thus making them sensitive to the cross-correlation method (Fig. 5). This is not the case for the Fe II model, which shows fewer yet stronger lines.

The cross-correlation was performed on the residual spectra $S_{\rm res}$ (see Sect. 4) as in Borsa et al. (2021), normalising the model to unity and thus preserving the flux information (e.g., Hoeijmakers et al. 2019). In our analysis, we zeroed out any lines that have strengths less than 1% of the maximum line strength within the modelled wavelength range (e.g., Hoeijmakers et al. 2019). We selected a step of 1 km s^{-1} and a velocity range [−300, 300] km s^{-1}. The spectra were divided into segments of 200 Å

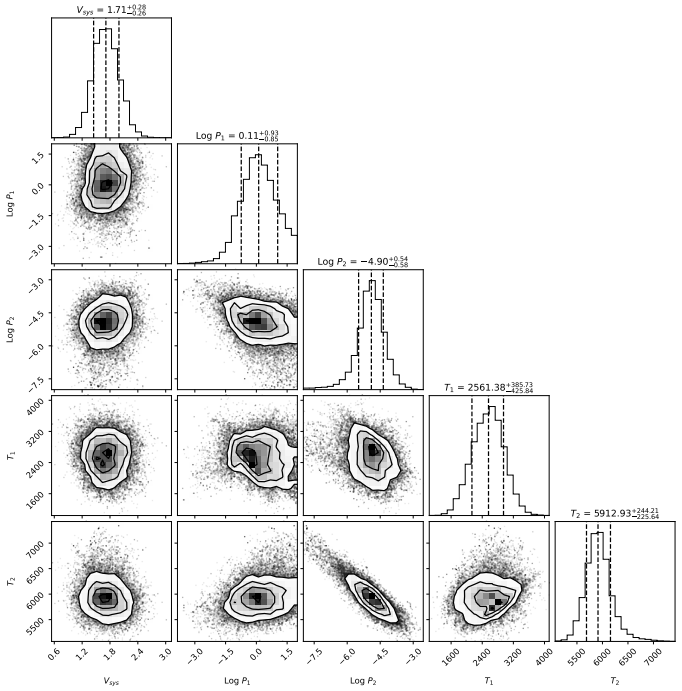

Fig. 4. Corner plot representing the posterior distribution of variables used for the DE-MCMC computations of the T-P profile parameters.

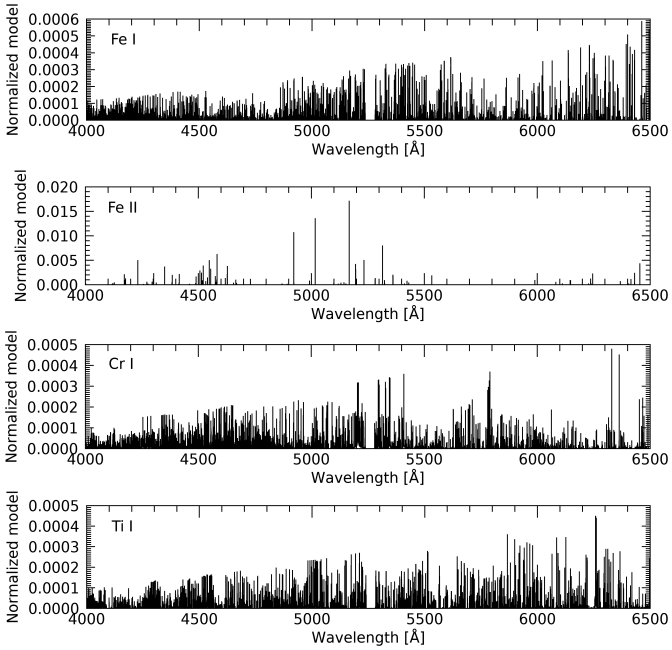

Fig. 5. Models used for the cross-correlations. *From top to bottom*: models of Fe I, Fe II, Cr I, and Ti I. The models are normalised to unity.

(e.g., Hoeijmakers et al. 2019), then the cross-correlation was performed for each segment covering the range 3900–6500 Å. We performed a 5σ clipping on the processed data frames to eliminate outliers and we masked the wavelength range 5240–5280 Å (i.e., the most affected by telluric contamination). Then for each exposure, we applied a weighted average of the cross-correlations of the single segments, where the weights applied to each segment were the square of the inverse of its standard deviation and the depths of the lines in the model.

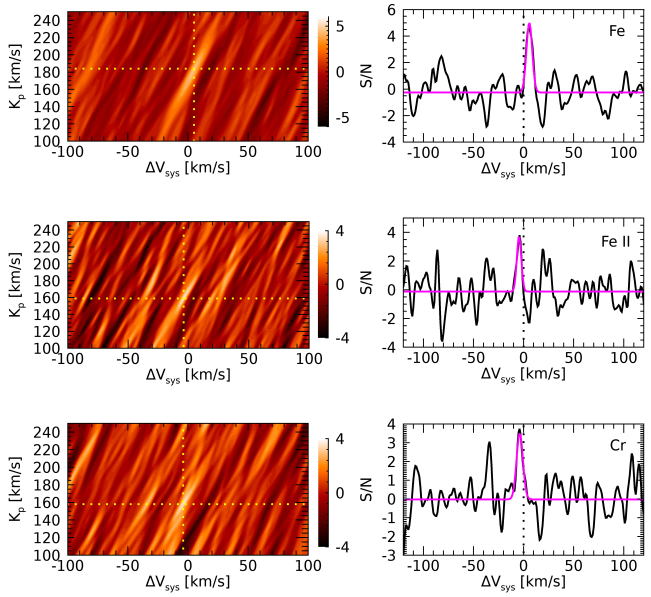

Fig. 6. Species detected in emission. From top to bottom: Detections of Fe I, Fe II, and Cr I in night 1. *Left panels* show the K_p-ΔV_{sys} maps, with the colour scale in S/N. The yellow dotted lines represent the best signal position. *Right panels* show the signal at the best K_p position, with a Gaussian fit shown in magenta.

For a range of K_p values from 0 to 300 km s^{-1}, in steps of 1 km s^{-1}, we averaged all the cross-correlation functions after shifting them in the planetary rest frame. This was done by subtracting the planetary radial velocity calculated for each spectrum as $v_p = K_p \times \sin 2\pi\phi$, with ϕ being the orbital phase. We thus created the K_p versus ΔV_{sys} maps to check that the signal is found close to the planet radial-velocity semi-amplitude and stellar systemic velocity, as is expected if the signal is of planetary origin. We then evaluated the noise by calculating the standard deviation of the K_p versus ΔV_{sys} maps far from where any stellar or planetary signal is expected. The S/N of the detections (Table 4) was calculated by dividing the best K_p cross-correlation function by the noise, and by fitting a Gaussian function to the result (see Fig. 6 for the detections of night 1).

The results indicate the detection of Fe I in both nights, with an S/N of 5.3 and 6.0, respectively. On the first night, we also detect Fe II with $S/N = 3.9$ and Cr I with $S/N = 3.6$. These two elements are not detected in night 2, while the level of noise is comparable to that of night 1. We do not detect Ti I. The results of the cross-correlations in individual nights and combining the two nights are reported in Table 4. We note that when combining the two nights, the S/N of the detections of Fe II and Cr I remains almost the same. This gives us further confidence as to the reliability of the planetary signal, as also without detection when adding the second night does not bring a strong destructive interference.

To assess the significance of our detections that we obtained in only one night, we also performed other statistical tests on this night only. The first one was performed by comparing the in-trail versus out-of-trail samples of the cross-correlation functions and performing a Welch t-test (e.g., Birkby et al. 2017; Nugroho et al. 2017; Brogi et al. 2018; Guilluy et al. 2019). To avoid oversampling, we resampled the cross-correlation functions to 1.5 km s^{-1}, which is about twice the average pixel size of the instrument (~0.8 km s^{-1}, Cosentino et al. 2014) and close to

Table 4. Results of the cross-correlation with theoretical models.

	Night 1			Night 2			Combined
Element	K_p [km s^{-1}]	ΔV_{sys} [km s^{-1}]	S/N	K_p [km s^{-1}]	ΔV_{sys} [km s^{-1}]	S/N	S/N
Fe I	184^{+5}_{-10}	5^{+3}_{-2}	5.3	176^{+3}_{-3}	1^{+2}_{-2}	6.0	7.1
Fe II	159^{+5}_{-4}	-4^{+2}_{-2}	3.9	ND	ND	ND	3.3
Cr I	158^{+6}_{-5}	-1^{+2}_{-3}	3.6	ND	ND	ND	3.5

Notes. ND stands for no detection.

Table 5. Significance of the detections in night 1 calculated with different statistical methods.

Element	S/N	T-test	KS	Bootstrap
Fe I	5.3	6.8σ	5.4σ	5.9σ
Fe II	3.9	3.2σ	3.1σ	3.6σ
Cr I	3.6	3.9σ	3.1σ	3.1σ

its half-width at half maximum (~1.3 km s^{-1}). For each species tested, we selected the interval $20 < |v| < 100$ km s^{-1} for the out-of-trail sample, while for the in-trail one we optimised the width choosing the one that maximises the detection. We observed, in any case, a low dependence of the final significance on the width of the in-trail sample. The error bars on the two samples were calculated as the square root of the number of data points in each bin (Fig. B.1). This test gives a confidence of 6.8, 3.2, and 3.9σ for Fe I, Fe II, and Cr I, respectively, that the in-trail and out-of-trail distributions are drawn from different parent distributions in night 1. The distributions are compatible with Gaussian functions, calculated by assuming the average of the samples and their standard deviation as the centre and the width of the Gaussian, respectively (Fig. B.1), thus validating the use of these statistics. We note, however, that Cabot et al. (2019) suggest that the Welch t-test could sometimes overestimate the confidence of detections. We thus also performed Kolmogorov-Smirnov (KS) statistics on the same distributions, obtaining a confidence of 5.4, 3.1, and 3.1σ for Fe I, Fe II, and Cr I, respectively, that the in- and out-of-trail distributions are different (Table 5).

We carried out a further statistic significance test by performing a bootstrap, adapting the method proposed in Appendix C.2 of Hoeijmakers et al. (2020b) to our dataset, where there is no transit. For each species, we shifted each cross-correlation function of the time series to a random radial velocity taken from a uniform distribution, masking all the zones where the planetary signal is expected, and averaged these CCFs. We then fitted a Gaussian profile with a fixed width of 5, 10, or 20 km s^{-1}, centred at a random position in the averaged CCF. This was repeated 100 000 times for each species. In Fig. B.2 we show the resulting distributions coming from random fluctuations for night 1, together with the contrast of the detections, which are significantly stronger. We fitted a Gaussian function to each of the random distributions, took the maximum width σ of the three (which is always the one created with a fixed width of 5 km s^{-1}), and estimated the significance of detection by taking the ratio between the amplitude of the signal and σ (Table 5). We confirm the detections of Fe I, Fe II, and Cr I in night 1 with all the statistical methods used, thus validating their robustness. Following the detection of multiple species, we further investigated the presence of V I, V II, Y I, Ca I, Mg I, AlO, TiO, and VO, but without finding statistical significance for their presence in the planetary atmosphere.

Table 6. Results of the T-P profile retrieval for the single nights.

Parameter	Night 1	Night 2	Unit
ΔV_{sys}	$2.80^{+0.45}_{-0.41}$	$1.40^{+0.29}_{-0.28}$	km s^{-1}
$\log_{10} P_1$	$-0.86^{+1.36}_{-0.96}$	$-0.11^{+1.39}_{-1.34}$	log bar
T_1	$2508.67^{+278.96}_{-282.96}$	$2610.47^{+229.20}_{-303.27}$	K
$\log_{10} P_2$	$-3.36^{+0.47}_{-0.60}$	$-5.25^{+0.67}_{-0.74}$	log bar
T_2	$5561.58^{+195.52}_{-149.86}$	$6139.38^{+250.69}_{-287.50}$	K

6. Discussion and conclusions

Our result confirms the tendency of a temperature inversion in the atmosphere of UHJs caused by the absorption of UV and optical stellar light by metals. KELT-20b is the fourth UHJ for which dayside neutral iron emission is detected with high-resolution spectroscopy. All these planets orbit A-type stars. Lothringer & Barman (2019) theoretically show that the slope of the T-P and the temperature range across the temperature inversion in UHJs both increase as the host star effective temperature increases. This is thus probably the reason that all the detections of temperature inversion with high-resolution spectroscopy up to now have been for UHJs orbiting A-type stars. These stars have strong UV emission, which is the wavelength range where the metals causing temperature inversions present the largest number of lines (Fossati et al. 2021).

We added Cr I to the species discovered in emission from the dayside of an exoplanet by performing a multi-species atomic detection of planetary emission. We note that we detected Fe II and Cr I only after occultation, while we saw Fe I better before the occultation. In principle, the S/N is almost the same for both nights, so this could hint at different atmospheric properties in the atmosphere at sight during the different orbital phases. An offset in thermal phase curves has often been observed for short-period exoplanets (e.g., Deming & Knutson 2020, and references therein), so one possibility is that the temperature (or temperature gradient) is higher in the atmosphere in view after the occultation, making Fe to become more ionised and Cr I emission visible.

We tried to verify this by performing a further retrieval of the T-P profile in the same way as in Sect. 4, but separately before and after occultation. While the differences are not highly significant, the results point to a steeper thermal inversion for night 1, after the occultation, where we have detections of multiple species (Figs. 7, B.3, B.4, Table 6). It must be noted that our assumption of the T-P profile might be oversimplified and could not represent the true conditions of the atmosphere.

The emission at different planetary phases could be used to constrain the atmospheric dynamics of the planet (e.g. Arcangeli et al. 2021), but an in-depth analysis of different planetary phases however requires a framework of analysis that includes

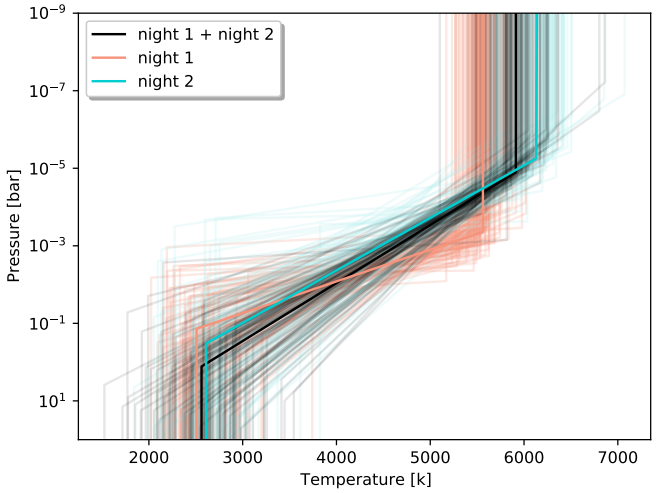

Fig. 7. T-P profile retrieved for nights 1 and 2. Thinner lines represent 100 T-P profiles randomly extracted from the MCMC posteriors.

3D atmospheric modelling. To verify the real atmospheric origin of the differences found, it will be useful to collect more data with a high S/N to check the repeatability of the behaviour and possibly give a stronger constraint on the T-P profiles directly from the observations. After the submission of our work, Si I dayside emission was detected from the planet (Cont et al. 2022), and a strong temperature inversion consistent with our results was retrieved in its atmosphere using Fe I templates (Yan et al. 2022). Temperature inversion was also retrieved detecting H_2O and CO emission features at low resolution (Fu et al. 2022). Detections of Fe II and Cr I are firstly presented in this work.

This work demonstrates that high-resolution emission spectroscopy can be exploited similar to high-resolution transmission spectroscopy for multiple species' detection in exoplanetary atmospheres. This allows us to investigate the dynamical, chemical, and radiative processes operating in UHJ atmospheres.

Acknowledgements. We thank the referee for the useful comments that helped improving the work. We acknowledge the support by INAF/Frontiera through the "Progetti Premiali" funding scheme of the Italian Ministry of Education, University, and Research and from PRIN INAF 2019.

References

Arcangeli, J., Désert, J.-M., Line, M. R., et al. 2018, ApJ, 855, L30
Arcangeli, J., Désert, J.-M., Parmentier, V., et al. 2021, A&A, 646, A94
Baxter, C., Désert, J.-M., Parmentier, V., et al. 2020, A&A, 639, A36
Bell, T. J., & Cowan, N. B. 2018, ApJ, 857, L20
Birkby, J. L., de Kok, R. J., Brogi, M., et al. 2017, AJ, 153, 138
Borsa, F., Scandariato, G., Rainer, M., et al. 2015, A&A, 578, A64
Borsa, F., Rainer, M., Bonomo, A. S., et al. 2019, A&A, 631, A34
Borsa, F., Allart, R., Casasayas-Barris, N., et al. 2021, A&A, 645, A24
Brogi, M., Giacobbe, P., Guilluy, G., et al. 2018, A&A, 615, A16
Cabot, S. H. C., Madhusudhan, N., Hawker, G. A., et al. 2019, MNRAS, 482, 4422
Casasayas-Barris, N., Pallé, E., Yan, F., et al. 2018, A&A, 616, A151
Casasayas-Barris, N., Pallé, E., Yan, F., et al. 2019, A&A, 628, A9
Claudi, R., Benatti, S., Carleo, I., et al. 2017, Euro. Phys. J. Plus, 132, 364
Cont, D., Yan, F., Reiners, A., et al. 2022, A&A, 657, L2
Cosentino, R., Lovis, C., Pepe, F., et al. 2014, Proc. SPIE, 9147, 91478C
Deming, D., & Knutson, H. A. 2020, Nat. Astron., 4, 453
Eastman, J., Gaudi, B. S., & Agol, E. 2013, PASP, 125, 923
Ehrenreich, D., Lovis, C., Allart, R., et al. 2020, Nature, 580, 597
Fortney, J. J., Lodders, K., Marley, M. S., et al. 2008, ApJ, 678, 1419
Fossati, L., Shulyak, D., Sreejith, A. G., et al. 2020, A&A, 643, A131
Fossati, L., Young, M. E., Shulyak, D., et al. 2021, A&A, 653, A52
Fu, G., Sing, D. K., Lothringer, J. D., et al. 2022, ApJ, 925, L3
Giacobbe, P., Brogi, M., Gandhi, S., et al. 2021, Nature, 592, 205
Gibson, N. P., Merritt, S., Nugroho, S. K., et al. 2020, MNRAS, 493, 2215
Guilluy, G., Sozzetti, A., Brogi, M., et al. 2019, A&A, 625, A107
Guilluy, G., Andretta, V., Borsa, F., et al. 2020, A&A, 639, A49
Hoeijmakers, H. J., Ehrenreich, D., Kitzmann, D., et al. 2019, A&A, 627, A165
Hoeijmakers, H. J., Cabot, S. H. C., Zhao, L., et al. 2020a, A&A, 641, A120
Hoeijmakers, H. J., Seidel, J. V., Pino, L., et al. 2020b, A&A, 641, A123
Hubeny, I., Burrows, A., & Sudarsky, D. 2003, ApJ, 594, 1011
Kasper, D. H., Bean, J. L., Line, M. R., et al. 2021, ApJ, 921, L18
Kesseli, A. Y., Snellen, I. A. G., Alonso-Floriano, F. J., et al. 2020, AJ, 160, 228
Lothringer, J. D., & Barman, T. 2019, ApJ, 876, 69
Lothringer, J. D., Barman, T., & Koskinen, T. 2018, ApJ, 866, 27
Lund, M. B., Rodriguez, J. E., Zhou, G., et al. 2017, AJ, 154, 194
Mollière, P., Wardenier, J. P., van Boekel, R., et al. 2019, A&A, 627, A67
Nugroho, S. K., Kawahara, H., Masuda, K., et al. 2017, AJ, 154, 221
Nugroho, S. K., Gibson, N. P., de Mooij, E. J. W., et al. 2020a, ApJ, 898, L31
Nugroho, S. K., Gibson, N. P., de Mooij, E. J. W., et al. 2020b, MNRAS, 496, 504
Parmentier, V., Line, M. R., Bean, J. L., et al. 2018, A&A, 617, A110
Pino, L., Désert, J.-M., Brogi, M., et al. 2020, ApJ, 894, L27
Rainer, M., Borsa, F., Pino, L., et al. 2021, A&A, 649, A29
Saffe, C., Miquelarena, P., Alacoria, J., et al. 2021, A&A, 647, 49
Scandariato, G., Borsa, F., Sicilia, D., et al. 2021, A&A, 646, A159
Snellen, I. A. G., Albrecht, S., de Mooij, E. J. W., & Le Poole, R. S. 2008, A&A, 487, 357
Stangret, M., Casasayas-Barris, N., Pallé, E., et al. 2020, A&A, 638, A26
Talens, G. J. J., Justesen, A. B., Albrecht, S., et al. 2018, A&A, 612, A57
Ter Braak, C. J. F. 2006, Stat. Comput., 16, 239
Vidal-Madjar, A., Arnold, L., Ehrenreich, D., et al. 2010, A&A, 523, A57
Yan, F., Pallé, E., Reiners, A., et al. 2020, A&A, 640, L5
Yan, F., Reiners, A., Pallé, E., et al. 2022, A&A, 659, A7

Appendix A: Parameters

Table A.1. Physical and orbital parameters of the KELT-20 system used in this work.

Parameter	Value	Reference
	Stellar Parameters	
$T_{\rm eff}$	8980^{+90}_{-130} K	1
$v \sin i$	116.23 ± 1.25 km s^{-1}	2
$M_\star$	$1.89^{+0.06}_{-0.05}$ $M_\odot$	1
$R_\star$	1.60 ± 0.06 $R_\odot$	1
	Planetary parameters	
$M_{\rm p}$	< 3.51 $M_{\rm Jup}$	3
$R_{\rm p}$	1.83 ± 0.07 $R_{\rm Jup}$	1
$T_{\rm eq}$	2260 ± 50 K	1
	Orbital parameters	
T_0	$7909.5906^{+0.0003}_{-0.0002}$ BJD-2450000	1
P	$3.474119^{+0.000005}_{-0.000006}$ days	1
e	0	fixed
$K_{\rm s}$	322.51* m s^{-1}	4
$K_{\rm p}$	175* km s^{-1}	
$V_{\rm sys}$	-24.48 ± 0.04 km s^{-1}	2

*Assuming the upper mass limit for the planet.

References. [1] Talens et al. (2018); [2] Rainer et al. (2021); [3] Lund et al. (2017); [4] Casasayas-Barris et al. (2019)

Appendix B: Statistics

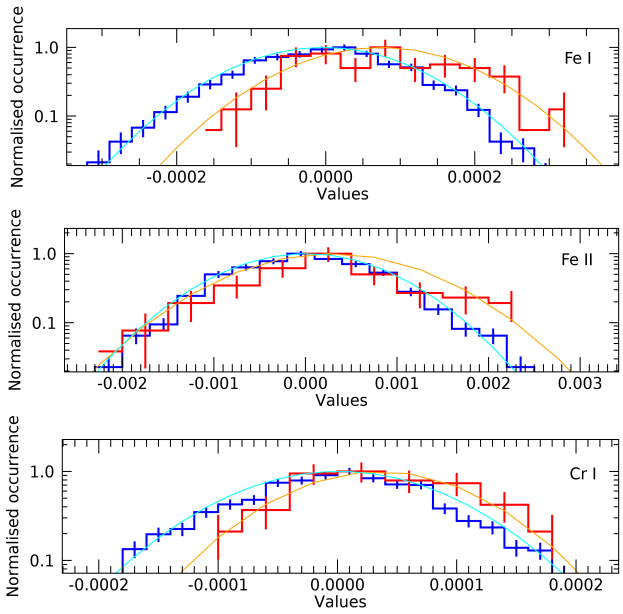

Fig. B.1. Distribution of the night 1 in-trail and out-of-trail samples for Fe I, Fe II, and Cr I, respectively. The blue histogram represents the out-of-trail distribution, while the red histogram is the in-trail one. The respective Gaussian distributions are shown as cyan and orange lines.

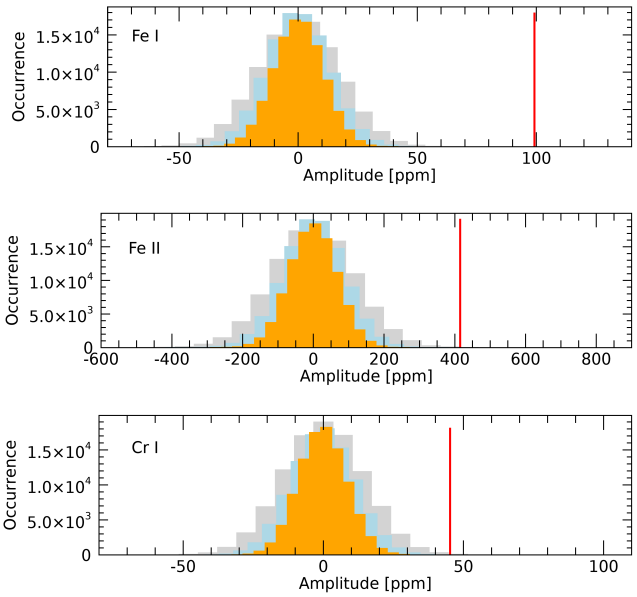

Fig. B.2. Distributions created with the bootstrap method for Fe I, Fe II, and Cr I, respectively. The grey, light blue, and orange distributions come from fixed widths of 5, 10, and 20 km s^{-1}, respectively. The vertical red lines show the amplitude of the detection.

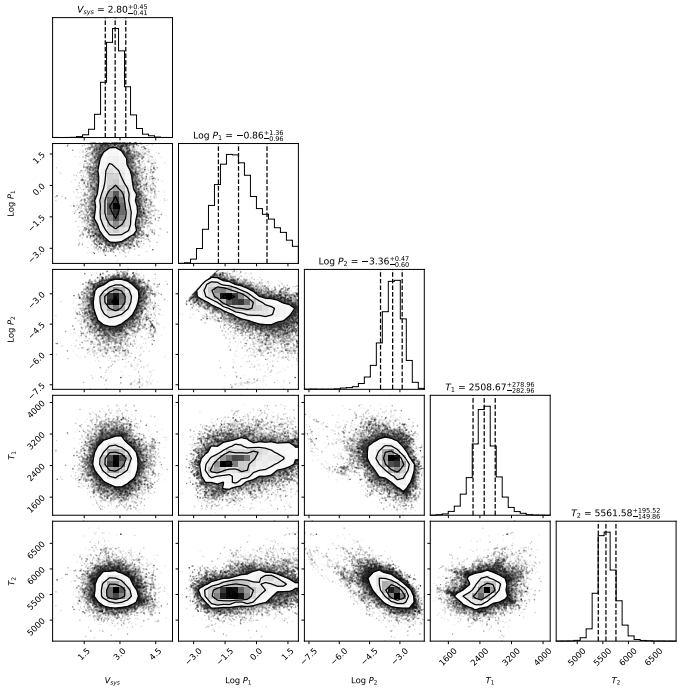

Fig. B.3. Corner plot representing the posterior distribution of variables used for the DE-MCMC computations of the T-P profile parameters for night 1.

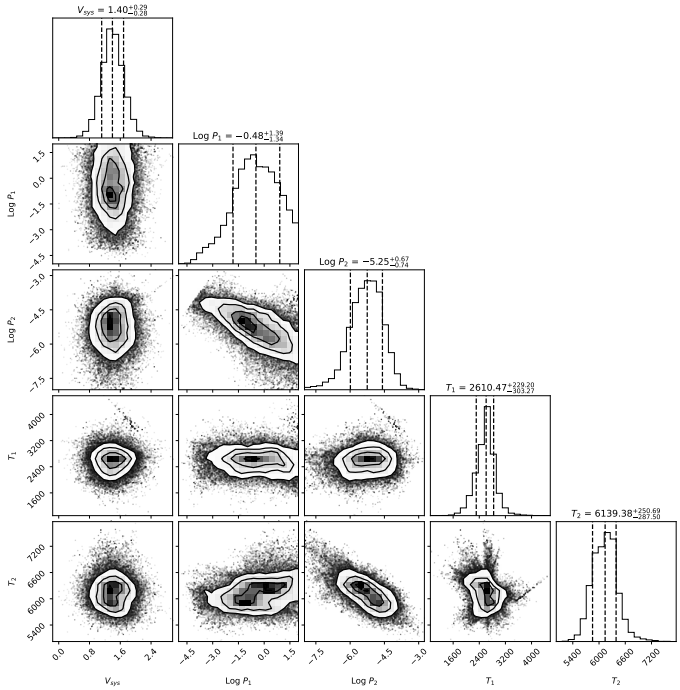

Fig. B.4. Corner plot representing the posterior distribution of variables used for the DE-MCMC computations of the T-P profile parameters for night 2.